Tetrairon(II)-based Extended Metal Atom Chains as Single-Molecule Magnets

*Alessio Nicolini,[a,b] Marco Affronte,[b] Daniel J. SantaLucia,[c] Marco Borsari,[a] Benjamin Cahier,[d] Matteo Caleffi,[b] Antonio Ranieri,[e] John F. Berry,[c] and Andrea Cornia[a]**

[a]Department of Chemical and Geological Sciences, University of Modena and Reggio Emilia & INSTM, I-41125 Modena, Italy

[b]Department of Physics, Informatics and Mathematics, University of Modena and Reggio Emilia, I-41125 Modena, Italy

[c]Department of Chemistry, University of Wisconsin-Madison, 1101 University Avenue, Madison, Wisconsin 53706, United States

[d]Max-Planck-Institut für Kohlenforschung, Kaiser-Wilhelm-Platz 1, 45470 Mülheim an der Ruhr, Germany

[e]Department of Life Sciences, University of Modena and Reggio Emilia, I-41125 Modena, Italy

Electronic Supplementary Information

1) MALDI-TOF-MS

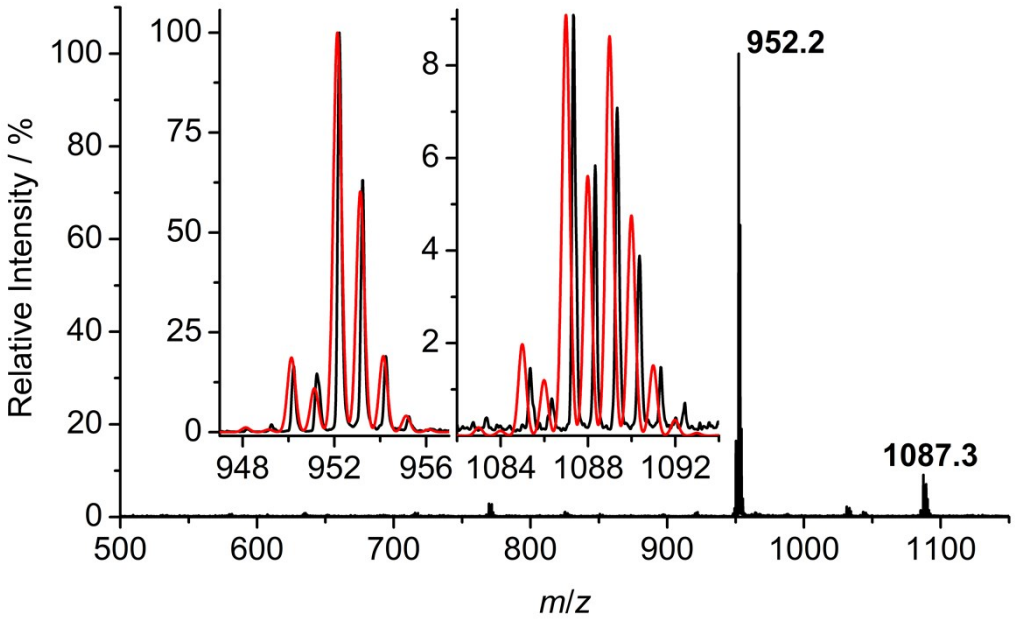

Figure S1. MALDI-TOF-MS spectrum of crude **1Br** in positive ion mode. The inset shows the experimental (black line) and simulated (red line) isotopic patterns of the peaks at *m*/*z* = 952.2 ($[Fe_3(tpda)_3+H]^+$) and 1087.3 ($[Fe_4(tpda)_3Br+H]^+$).

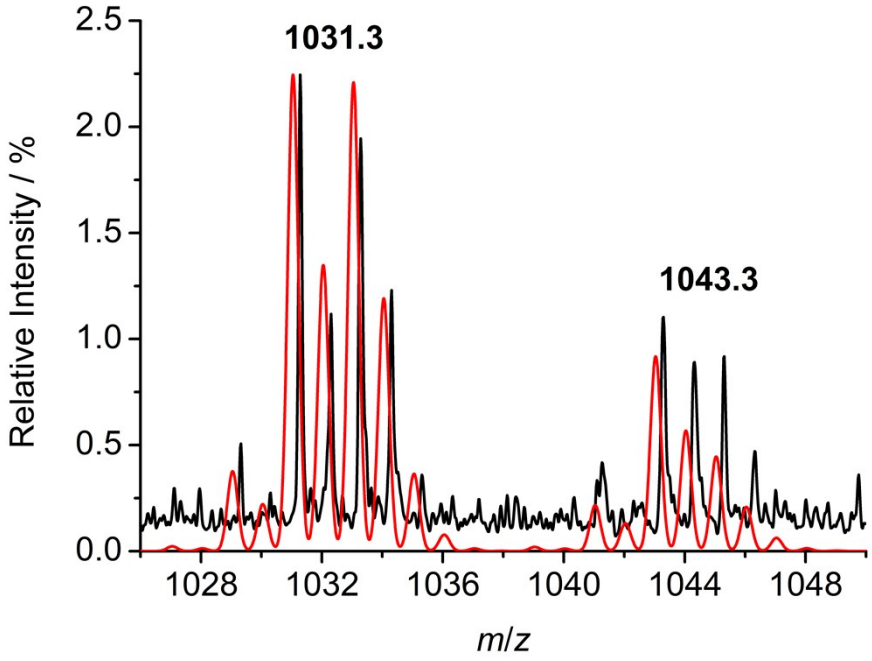

Figure S2. Magnification between *m*/*z* = 1026 and 1050 of the MALDI-TOF-MS spectrum of crude **1Br** in positive ion mode (black line). The red line represents the simulated isotopic pattern of the peaks at *m*/*z* = 1031.3 ($[Fe_3(tpda)_3Br+H]^+$) and 1043.3 ($[Fe_4(tpda)_3Cl+H]^+$).

2) ESI-MS

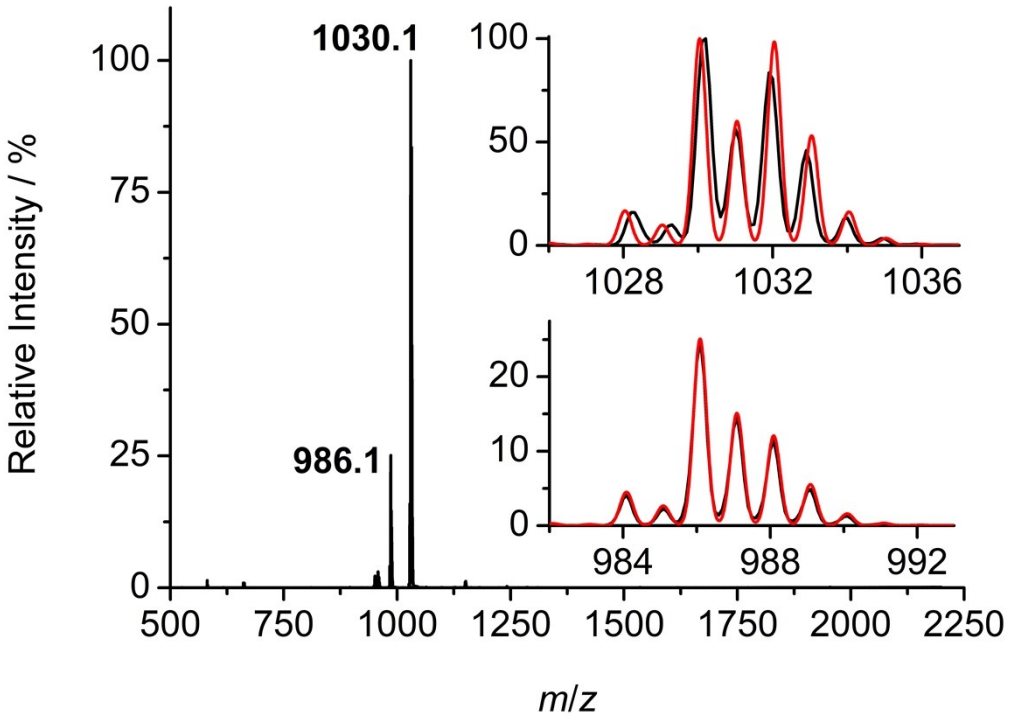

Figure S3. ESI-MS spectrum of **1Br** (direct infusion, CH_2Cl_2, positive ion mode). The inset shows the experimental (black line) and simulated (red line) isotopic patterns of the peaks at m/z = 1030.1 ($[Fe_3(tpda)_3Br]^+$) and 986.1 ($[Fe_3(tpda)_3Cl]^+$).

3) ^{1}H NMR Spectroscopy

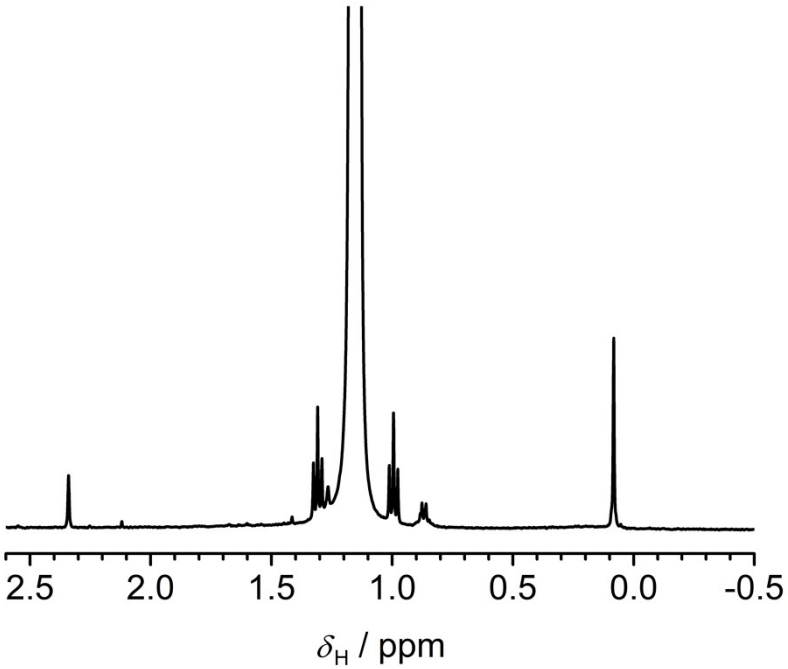

Figure S4. ^{1}H NMR spectrum of **1Br** in CD_2Cl_2 (298 K, 400.13 MHz) in the 0−2.6 ppm region. Processing parameters (TopSpin 4.0.6[1]): SI = TD, LB = 1.00 Hz. δ_H (ppm) = 0.08 (silicone grease, CH_3, s), 0.9 (H grease, CH_3, m), 1.15 (diethyl ether, CH_3, t, ^3J = 7 Hz), 1.27 (H grease, CH_2, br s), 2.12 (acetone, CH_3, s), 2.34 (toluene, CH_3, s).

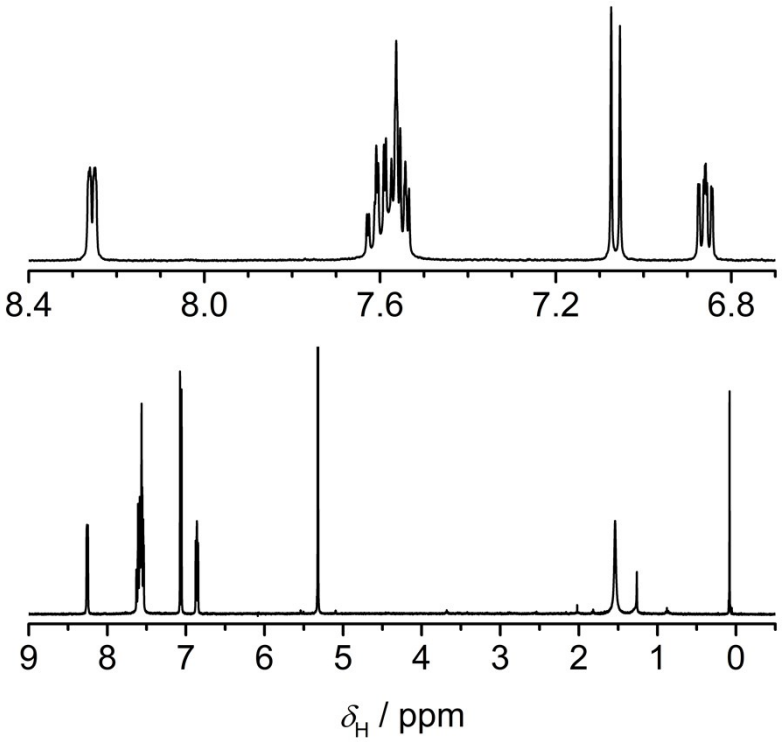

Figure S5. ^{1}H NMR spectrum of H_2tpda in CD_2Cl_2 (298 K, 400.13 MHz) up to δ_H = 9 ppm (bottom) and for δ_H = 6.7−8.4 ppm (above). Processing parameters (TopSpin 4.0.6[1]): SI = TD, LB = 0.30 Hz. δ_H (ppm) = 0.08 (silicone grease, CH_3, s), 0.9 (H grease, CH_3, m), 1.26 (H grease, CH_2, br s), 1.54 (water, OH, s), 5.32 (residual signal of CD_2Cl_2).

4) UV-Vis-NIR Spectroscopy

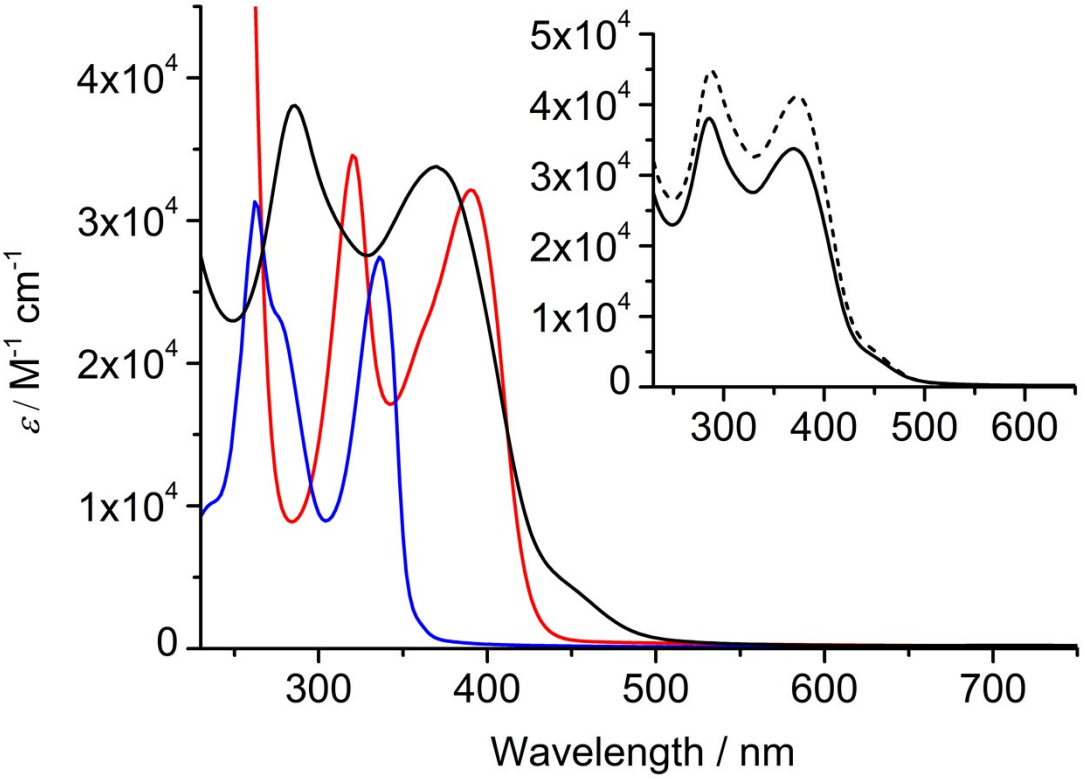

Figure S6. UV-Vis-NIR spectrum of **1Br** in CH_2Cl_2 (black line) and of H_2tpda in THF before (blue line) and after (red line) the addition of excess *t*BuOK. The inset shows a comparison between the spectra of **1Br** (solid line) and its chloro analogue **1Cl** (dashed line) in CH_2Cl_2. All the spectra were recorded up to 1500 nm, but only the characteristic portion of them is reported. The spectra of H_2tpda and **1Cl** are taken from Ref.[2]

5) Single Crystal X-Ray Diffraction

Supplementary Note 1: minority crystal phases. The described synthetic procedure affords minor amounts of other crystal phases, which are easily removed by flotation. These include:

a) small, yellow parallelogram-shaped plates, as-yet unidentified with certainty;

b) (occasionally) yellow elongated plates, identified as a second solvatomorph of **1Br**. Preliminary crystal data at 298(2): **1Br**·0.62CH_2Cl_2·0.38Et_2O, triclinic, $P\bar{1}$, a = 13.8989(8), b = 17.5023(8), c = 23.1212(13) Å, α = 95.9578(17), β = 101.9550(19), γ = 113.2249(16)°, V = 4947.8(5) Å^3, Z = 4, $R1$ ($I \geq 2\sigma(I)$) = 6.21%.

Supplementary Note 2: details of structural analysis for 1Br·2.3CH_2Cl_2·Et_2O. Indexing of intense peaks in the diffraction pattern gave a monoclinic P unit cell very similar to that of chloro derivative,[2] with a = 19.6801(16), b = 16.4420(14), c = 18.6092(14) Å, β = 104.979(3)°, V = 5817.0(8) Å^3, Z = 4, R_{merge} = 2.4% at 115(2) K. Systematic absences also hinted to the same space group ($P2_1/c$) although many violations were observed. Weak superstructure reflections were indeed detected at half-integer reciprocal-lattice points (h+1/2, k+1/2, l+1/2), with average intensity > 20 times lower than for substructure reflections. The complete diffraction pattern could be indexed using a metrically monoclinic C-centered cell with the same b-axis orientation as the monoclinic P cell, but a fourfold-larger volume (e.g.: **a**′ = 2**c**, **b**′ = 2**b**, **c**′ = –**a**–**c**, or alternative settings with a different choice of supercell vectors in the ac-plane; R_{merge} = 3.4%). Systematic absences however revealed that a c-type glide plane is not present in this supercell, thus restricting possible space groups to $C2$, Cm or $C2/m$. Since these space groups are inconsistent with the known crystal structure of the chloro derivative,[2] we argued that the structure cannot be monoclinic. This conclusion is supported by group-subgroups relations explorable with the program SUBGROUPS at the Bilbao Crystallographic Server (www.cryst.ehu.es). Application of a commensurate modulation with wave-vector q = (1/2, 1/2, 1/2) to the 13 monoclinic space groups affords superstructures that are either triclinic or belong to space groups $C2$, Cm or $C2/m$. In particular, monoclinic space groups compatible with the crystal structure of the chloro derivative (i.e. $P2_1/c$, $P2_1$ and Pc) give triclinic superstructures with doubled unit-cell volume [a = 23.3208(20), b = 24.8162(20), c = 24.8374(20) Å, α = 82.930(3), β = 64.239(3), γ = 64.270(3)°, V = 11623.9(17) Å^3, Z = 8, R_{merge} = 2.9%]. Unfortunately, refinement in space-group $P\bar{1}$ proved very difficult due to the four independent and partially disorderd tetrairon(II) molecules in the asymmetric unit and to the extensively disordered lattice solvent. The results suggested that the observed superstructure arises from a commensurate modulation of lattice solvent. On the contrary, refinement on substructure reflections converged well and was regarded as completely satisfactory for the purposes of the present study. The actual superstructure was therefore not further investigated. A second data collection at 115(2) K was carried out on a crystal from another synthetic batch and afforded a very similar diffraction pattern and an identical structure. *Five* additional prismatic crystals were screened, coming from both syntheses, and afforded the same unit-cell parameters.

Table S1. Crystal data and refinement parameters for **1Br**·2.3CH_2Cl_2·Et_2O.

Identification code	201117na_7_work3bis_complete
Empirical formula	$C_{51.29}H_{47.58}Br_2Cl_{4.63}Fe_4N_{15}O$
Formula weight	1437.22
Temperature (K)	115(2)
Crystal system	monoclinic
Space group	$P2_1/c$
a (Å)	19.6801(16)
b (Å)	16.4420(14)
c (Å)	18.6092(14)
α (deg)	90
β (deg)	104.979(3)
γ (deg)	90
Volume (Å^3)	5817.0(8)
Z	4
ρ_{calcd} (g cm^{-3})	1.641
μ (mm^{-1})	2.616
F(000)	2884.0
Crystal size (mm^3)	0.710 × 0.530 × 0.390
Radiation	Mo-Kα (λ = 0.71073 Å)
$2\theta_{min}/2\theta_{max}$ (deg)	4.286/56.072
Index ranges	$-24 \le h \le 26$, $-21 \le k \le 20$, $-24 \le l \le 24$
Reflections collected	61609
Independent reflections	14013 [R_{int} = 0.0245, R_{sigma} = 0.0202]
Data/restraints/parameters	14013/134/829
Goodness-of-fit on F^2	1.214
Final R indexes ($I \ge 2\sigma(I)$)	R_1 = 0.0606, wR_2 = 0.1489
Final R indexes (all data)	R_1 = 0.0664, wR_2 = 0.1520
Largest diff. peak/hole (e Å^{-3})	2.60/−0.99

Table S2. Interatomic distances (Å) and angles (deg) for **1Br**·2.3CH_2Cl_2·Et_2O.

Fe1−Fe2	2.9747(12)	Fe1A−Fe2A	2.890(10)
Fe2−Fe3	2.9711(11)	Fe2A−Fe3A	3.026(10)
Fe3−Fe4	2.9551(12)	Fe3A−Fe4A	2.954(11)
Fe1−Br1	2.5314(11)	Fe1A−Br1A	2.525(8)
Fe4−Br2	2.5100(12)	Fe4A−Br2A	2.499(8)
Fe1−N1	2.089(4)	Fe1A−N1	2.096(13)
Fe1−N2	2.067(4)	Fe1A−N2	2.293(12)
Fe1−N3	2.096(4)	Fe1A−N3A	2.04(2)
Fe2−N4	2.108(4)	Fe2A−N4	2.238(7)
Fe2−N5	1.993(4)	Fe2A−N5	2.176(7)
Fe2−N6	2.011(4)	Fe2A−N6A	2.05(2)
Fe2−N7	2.175(4)	Fe2A−N9A	2.198(19)
Fe2−N8	2.492(4)	Fe3A−N8	2.103(8)
Fe3−N8	2.500(4)	Fe3A−N9A	2.77(2)
Fe3−N9	2.234(4)	Fe3A−N10	1.946(9)
Fe3−N10	2.042(4)	Fe3A−N11	1.963(9)
Fe3−N11	2.036(4)	Fe3A−N12A	2.03(2)
Fe3−N12	2.087(4)	Fe4A−N13	2.065(17)
Fe4−N13	2.088(4)	Fe4A−N14	2.010(16)
Fe4−N14	2.088(4)	Fe4A−N15A	2.10(3)
Fe4−N15	2.071(5)		
Br1−Fe1−Fe2	177.01(6)	Br1A−Fe1A−Fe2A	176.2(6)
Fe1−Fe2−Fe3	172.08(4)	Fe1A−Fe2A−Fe3A	168.5(4)
Fe2−Fe3−Fe4	167.67(6)	Fe2A−Fe3A−Fe4A	169.9(5)
Fe3−Fe4−Br2	178.62(8)	Fe3A−Fe4A−Br2A	176.1(7)
Br1−Fe1−N1	95.07(11)	Br1A−Fe1A−N1	94.8(5)
Br1−Fe1−N2	97.96(11)	Br1A−Fe1A−N2	97.9(4)
Br1−Fe1−N3	98.44(13)	Br1A−Fe1A−N3A	94.7(7)
N13−Fe4−Br2	98.45(12)	N13−Fe4A−Br2A	97.4(5)
N14−Fe4−Br2	97.84(12)	N14−Fe4A−Br2A	94.5(5)
N15−Fe4−Br2	96.91(13)	N15A−Fe4A−Br2A	99.1(8)
N1−Fe1−N2	121.12(15)	N1−Fe1A−N2	111.0(5)
N1−Fe1−N3	110.87(16)	N1−Fe1A−N3A	125.7(10)
N2−Fe1−N3	123.32(16)	N2−Fe1A−N3A	120.3(11)
N13−Fe4−N14	112.63(17)	N13−Fe4A−N14	117.1(8)
N13−Fe4−N15	116.27(18)	N13−Fe4A−N15A	123.7(11)
N14−Fe4−N15	125.75(19)	N14−Fe4A−N15A	114.8(11)

Table S3. Bond-Valence Sum calculations on **1Br**·2.3CH_2Cl_2·Et_2O.[a]

Atom	Fe^{2+}	Fe^{3+}
Fe1	1.650	1.902
Fe2	1.895	2.228
Fe3	1.767	2.078
Fe4	1.680	1.933

[a]Bond-valence parameters (R_0; B) were taken from file bvparm2016.cif available at https://www.iucr.org/resources/data/datasets/bond-valence-parameters:
Fe^{2+}–N^{-3}(1.76; 0.37), Fe^{3+}–N^{-3}(1.82; 0.37), Fe^{2+}–Br^{-1}(2.21; 0.35), Fe^{3+}–Br^{-1}(2.22; 0.37).

6) Electrochemistry

Table S4. Thermodynamic contributions to $E^{\circ\prime}$ for **1Br** and **1Cl** in CH_2Cl_2 solution at −13 °C, using 0.1 M TBABr and TBACl, respectively, as supporting electrolytes.[a]

1Br	$E^{\circ\prime}$ / V (±0.002)	$\Delta S^{\circ\prime}_{rc}$ / J K^{-1} mol^{-1}	$\Delta H^{\circ\prime}_{rc}$ / kJ mol^{-1}	$T\Delta S^{\circ\prime}_{rc}$ / F	$-\Delta H^{\circ\prime}_{rc}$ / F
I	−0.890	233±11	147.2±2.2	0.606±0.029	−1.525±0.022
II	−0.745	136±8	107.7±2.1	0.366±0.021	−1.116±0.021
III	−0.443	140±7	79.6±1.9	0.377±0.019	−0.825±0.019
IV	−0.142	134±12	48.5±1.7	0.348±0.032	−0.701±0.017
1Cl					
I	−1.125	281±12	181.5±2.1	0.757±0.032	−1.881±0.021
II	−0.855	190±9	131.8±2.2	0.512±0.024	−1.366±0.022
III	−0.639	193±10	111.6±1.8	0.520±0.027	−1.156±0.018
IV	−0.323	190±12	80.5±1.1	0.512±0.032	−0.834±0.011

[a]Potential values and thermodynamic parameters are referenced to the ferrocenium/ferrocene redox couple.

Table S5. Comproportionation constants (T = −13 °C) and the corresponding enthalpic and entropic components for mixed oxidation states of **1Br** (**1Cl**) in CH_2Cl_2 solution, using 0.1 M TBABr (TBACl) as supporting electrolytes.[a]

	K_c	$\Delta H^{\circ\prime}_c$ / kJ mol^{-1}	$\Delta S^{\circ\prime}_c$ / J K^{-1} mol^{-1}
$(Fe_4)^{9+}$	$0.65\cdot10^3$ ($1.73\cdot10^5$)	−41.8 (−49.7)	−107.7 (−90.9)
$(Fe_4)^{10+}$	$7.21\cdot10^5$ ($1.55\cdot10^4$)	−28.2 (−20.2)	4.3 (2.8)
$(Fe_4)^{11+}$	$6.89\cdot10^5$ ($1.35\cdot10^6$)	−30.6 (−31.1)	−6.0 (−2.3)

[a]The average errors on K_c, $\Delta H^{\circ\prime}_c$, and $\Delta S^{\circ\prime}_c$ are ±12%, ±0.8 kJ mol^{-1} and ±1.6 J K^{-1} mol^{-1}, respectively.

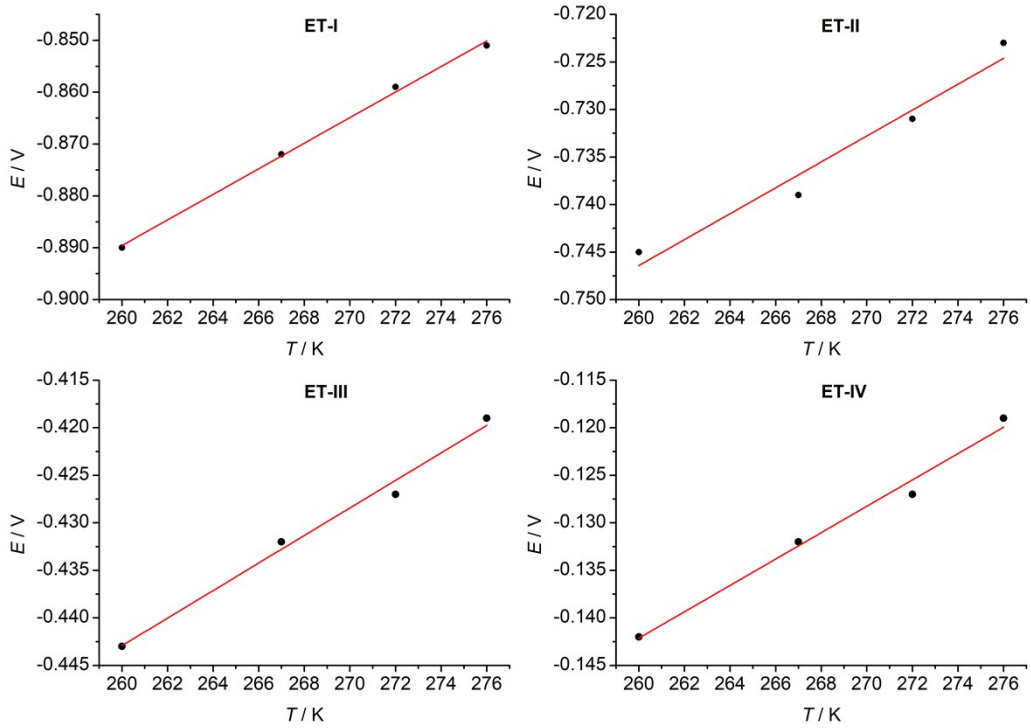

Figure S7. Plot of $E°'$ versus temperature for the different ET steps of $[Fe_4(tpda)_3Br_2]$ (**1Br**). Conditions: working electrode, GC; 0.1 M TBABr in CH_2Cl_2; scan rate, 0.05 V s^{-1}; reference, ferrocenium/ferrocene. The red lines represent the linear fits to the experimental datapoints.

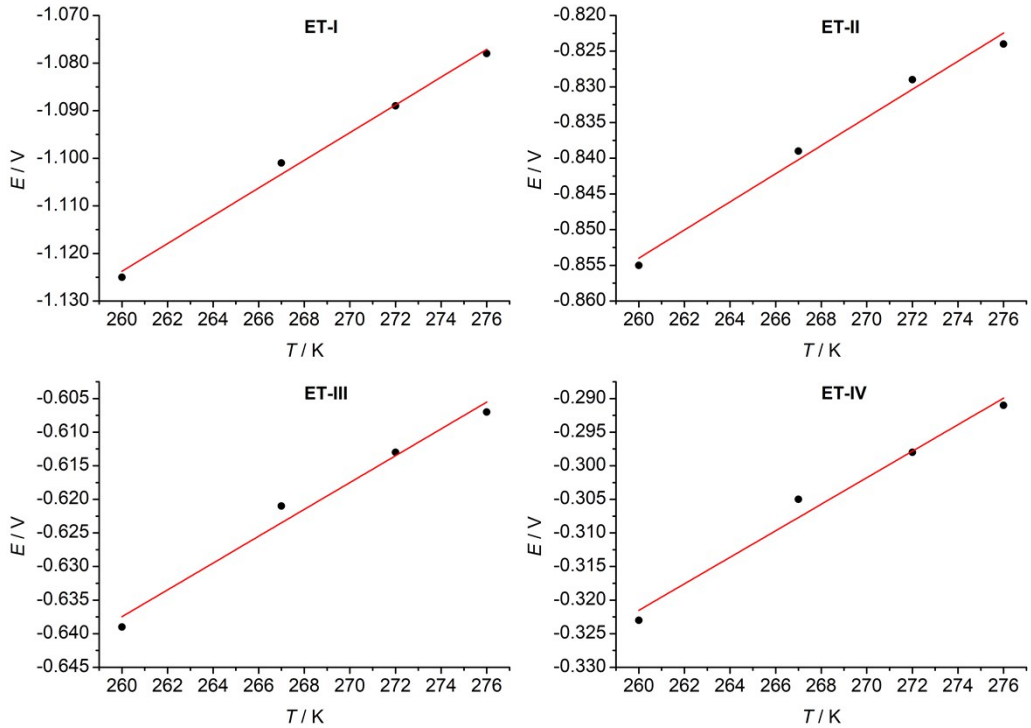

Figure S8. Plot of $E°'$ versus temperature for the different ET steps of $[Fe_4(tpda)_3Cl_2]$ (**1Cl**). Conditions: working electrode, GC; 0.1 M TBACl in CH_2Cl_2; scan rate, 0.05 V s^{-1}; reference, ferrocenium/ferrocene. The red lines represent the linear fits to the experimental datapoints.

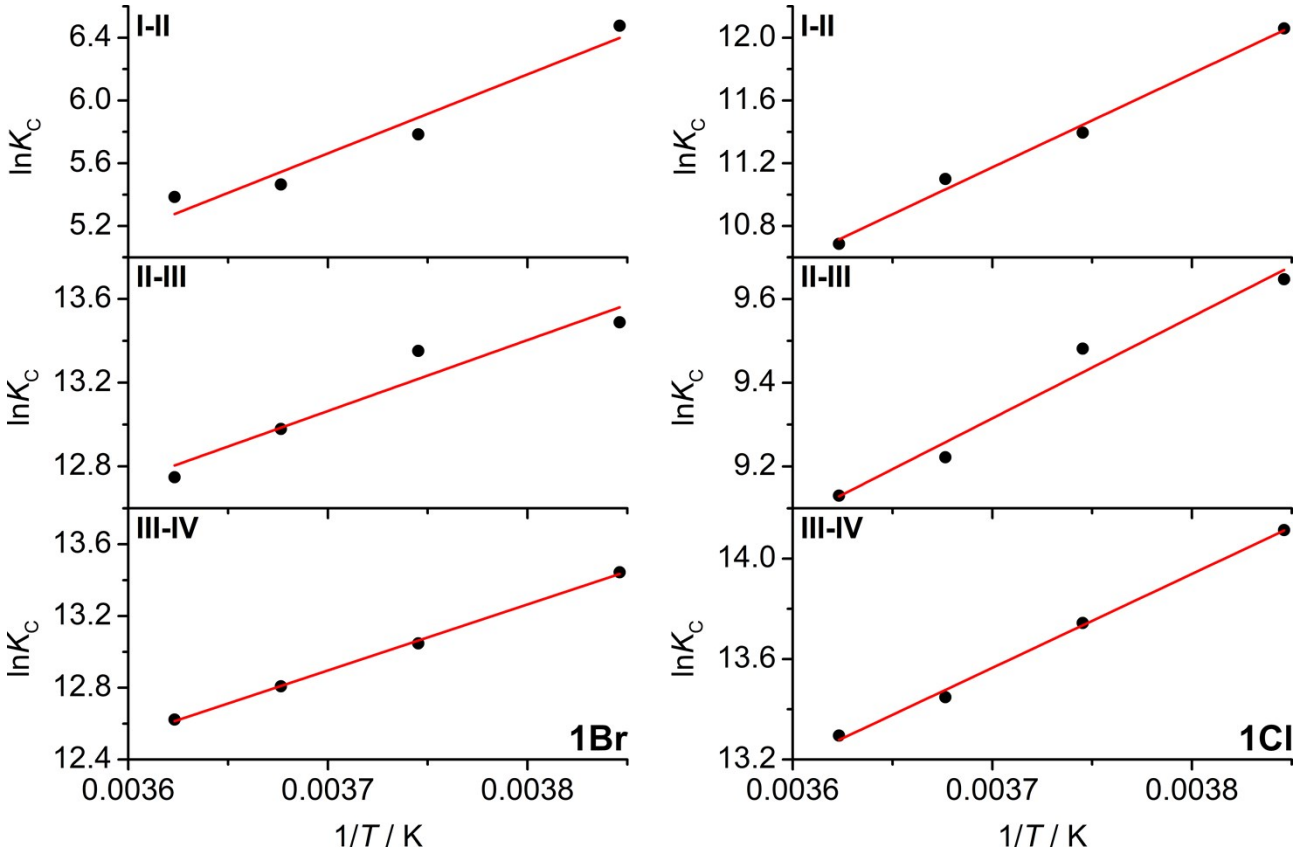

Figure S9. lnK_c vs 1/T (van't Hoff plots) for the mixed valence species derived from $[Fe_4(tpda)_3Br_2]$ (**1Br**, left panels) and $[Fe_4(tpda)_3Cl_2]$ (**1Cl**, right panels). The red lines represent the linear fits to the experimental datapoints.

7) Mössbauer Spectroscopy

Supplementary Note 3: fitting procedures. The reduced χ^2 value was used to assess the fit quality. The reduced χ^2 is defined as the χ^2 statistic per degree of freedom, where a degree of freedom is defined as the difference between the number of measured datapoints (n) and the number of parameters (p) fit to the data. The reduced χ^2 statistic is given by:

$$reduced\ \chi^2 = \frac{1}{n-p}\sum_{k=1}^{n}\frac{(O_k - E_k)^2}{E_k} \qquad \text{(S1)}$$

where O_k is the kth observed value for the signal intensity at a given source velocity and E_k is the kth expected value for the signal intensity at the same source velocity.[3]

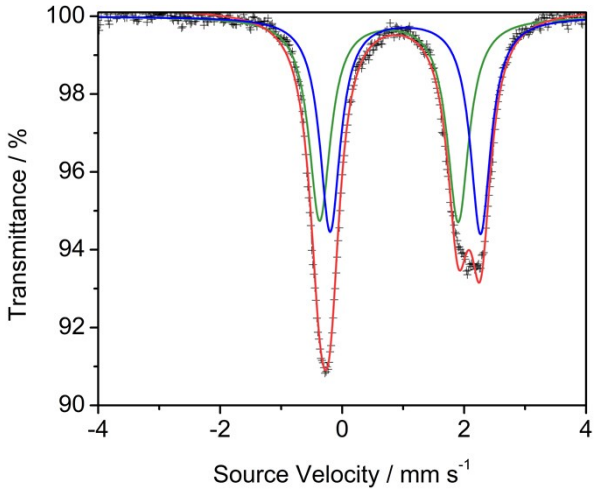

Figure S10. Alternative fit to the 77 K dataset for **1Cl**. Same color code as in Figure 6. Best-fit parameters: δ_1 = 0.77 mm/s, ΔE_{Q1} = 2.27 mm/s, $FWHM_1$ = 0.43 mm/s, δ_2 = 1.04 mm/s, ΔE_{Q2} = 2.47 mm/s, and $FWHM_2$ = 0.41 mm/s; reduced χ^2 = 1.697.

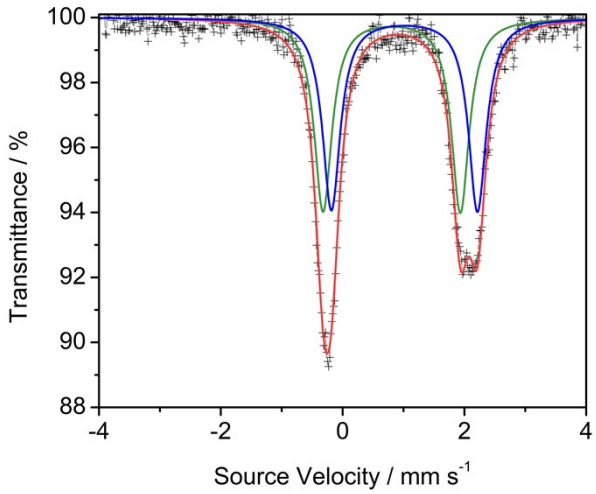

Figure S11. Alternative fit to the 77 K dataset for **1Br**. Same color code as in Figure 7. Best-fit parameters: δ_1 = 0.81 mm/s, ΔE_{Q1} = 2.25 mm/s, $FWHM_1$ = 0.35 mm/s, δ_2 = 1.01 mm/s, ΔE_{Q2} = 2.40 mm/s, and $FWHM_2$ = 0.35 mm/s; reduced χ^2 = 0.577.

8) AOM Calculations

Supplementary Note 4: AOM calculations. AOM calculations on **1Br** were carried out with the AOMX program package,[4] following the same approach used in Ref.[2] for chloro derivative **1Cl**. Since Fe1 and Fe4 exhibit very similar coordination environments (see Figure 4), their X-ray coordination geometries were averaged and, additionally, C_{3v} symmetry was enforced on the resulting average FeN_3Br chromophore to give Fe−N = 2.0832 Å, Fe−Br = 2.5207 Å and N−Fe−Br = 97.445°. This choice is justified by the observation that the magnetic response predicted by the AOM for the average C_{3v} chromophore in **1Cl** is within 0.5% from those of the real Fe1(N1,N2,N3,Cl1) and Fe4(N13,N14,N15,Cl2) chromophores.[2] Regarding the internal Fe centers Fe2 and Fe3 (see Figure 4), the X-ray coordination geometries of the chromophores Fe2(N4,N5,N6,N7,N8) and Fe3(N8,N9,N10,N11,N12) were directly used.

LF parameters e_σ and e_π that account for σ and π interactions, respectively,[5] were inferred from the values reported for *trans*-$[Fe(py)_4Br_2]$ and *trans*-$[Fe(py)_4(NCS)_2]$ (py = pyridine), which possess a tetragonally-elongated octahedral geometry. Based on spectroscopic data at 23 K, Little and Long[6] found $e_\sigma(py)$ = 4050 cm^{-1} and $e_\sigma(Br)$ = 2400 cm^{-1} in *trans*-$[Fe(py)_4Br_2]$ (Fe−N = 2.2059−2.270 Å, Fe−Br = 2.6753 Å).[7] In addition, anisotropic π interactions perpendicular to the aromatic plane, described by parameter $e_{\pi\perp}(py)$, must be taken into account for pyridine ligands. $e_{\pi\perp}(py)$ is usually very small in iron(II) complexes and a value of only ~100 cm^{-1} is reported in *trans*-$[Fe(py)_4(NCS)_2]$.[8] For the terminal Fe centers (Fe1 and Fe4) the nodal planes of pyridine π orbitals were taken to coincide with the Fe1–N1–C1, Fe1–N2–C16, Fe1–N3–C31, Fe4–N13–C15, Fe4–N14–C30 and Fe4–N15–C45 planes (Ψ = 155.917° in the idealized C_{3v} chromophore). It was assumed that π interactions for the axial bromide ligands, $e_\pi(Br)$, are isotropic in the plane perpendicular to the Fe−Br bond and amount to 30% of the corresponding σ contribution.[5]

For each ligand, the LF parameters were calculated from the above reference values assuming a r^{-6} dependence on metal-ligand distance r,[6–8] as given by:

$$e_t(X)' = e_t(X)\left(\frac{r}{r'}\right)^6 \qquad \text{(S2)}$$

where $t = \sigma$ or π and X is the type of ligand. In our previous AOM analysis of **1Cl** we used *trans*-$[Fe(py)_4Cl_2]$ as a reference compound with Fe−N = 2.229 Å.[9] In their paper, Little and Long[6] assumed the same $e_\sigma(py)$ value for *trans*-$[Fe(py)_4Br_2]$ and *trans*-$[Fe(py)_4Cl_2]$. Since the average Fe−N distances in the two compounds differ by 0.4% only (2.238 vs 2.229 Å), for the sake of simplicity and for a better comparison between **1Cl** and **1Br** we used Fe−N = 2.229 Å as reference distance for **1Br** as well, yielding $e_\sigma(py)$ = 6078 cm^{-1} and $e_{\pi\perp}(py)$ = 150 cm^{-1}. From the value of $e_\sigma(Br)$ = 3430 cm^{-1} we finally calculated $e_\pi(Br) = 0.3e_\sigma(Br)$ = 1029 cm^{-1}.

Racah parameters for the interelectronic repulsion were fixed at B = 850 cm^{-1} and C = 3100 cm^{-1}, hence ~20% lower than in free Fe^{2+}.[10] To assess the effects of SO coupling, the effective one-electron SO coupling constant (ζ_{3d}) was either neglected or fixed at 350 cm^{-1} in separate calculations for each chromophore, while the orbital reduction factor (k) was taken isotropic and unitary.[8]

AOM calculations on the terminal C_{3v} chromophore in zero magnetic field were performed both with and without the inclusion of SO coupling. In the first case (ζ_{3d} = 0), the ground ^5D Russell-Saunders term of the free Fe^{2+} ion (L = 2, S = 2) is split by the LF of three py and one bromido ligands into the three spin-quintet terms listed in Table S6. The ground ^5E term is well-isolated from the excited ones (> 6200 cm^{-1}) and consists in a 0.920:0.080 mixture of $(xz,yz)^3(xy,x^2–y^2)^2(z^2)^1$ and $(xz,yz)^2(xy,x^2–y^2)^3(z^2)^1$ configurations. The excited ^5E term corresponds to the complementary 0.080:0.920 mixture. Finally, the $^5A_1$ term coincides with the pure $(xz,yz)^2(xy,x^2–y^2)^2(z^2)^2$ configuration. When SO coupling is included in the calculation (ζ_{3d} = 350 cm^{-1}), the spin-quintet terms give the $(2L+1)(2S+1)$ = 25 zero-field levels listed in Table S6. The first ten low-lying levels are well-isolated (> 6000 cm^{-1}) from the remaining ones, and originate primarily from the ground

orbital doublet term ^{5}E. Using PHI v3.0.6 code[11] and the Simplex minimization algorithm, these levels were mapped onto the Griffith-Figgis Hamiltonian for the terminal irons (i = 1, 4):

$$\hat{H}_i = \hat{H}_{CF,i} + \lambda_i k_i \hat{\mathbf{L}}_i \cdot \hat{\mathbf{S}}_i + \mu_B \mathbf{B} \cdot \left(k_i \hat{\mathbf{L}}_i + g_e \hat{\mathbf{S}}_i\right) \quad \text{(S3)}$$

$$\hat{H}_{CF,i} = B^0_{2,i}\hat{O}^0_{2,i} + B^0_{4,i}\hat{O}^0_{4,i} + B^3_{4,i}\hat{O}^3_{4,i} \quad \text{(S4)}$$

where $\hat{\mathbf{L}}_i$ and $\hat{\mathbf{S}}_i$ are the orbital and spin angular momenta (L_i = 2, S_i = 2), **B** is the applied magnetic field, k_i is the orbital reduction factor, $\lambda_i = -\zeta_{3d}/2S_i$ is the effective many-electron SO coupling constant, μ_B is the Bohr magneton, and g_e is the electron g-factor. In accordance with the treatment in Ref.[8] we set k_i = 1 and $\lambda_i = -\zeta_{3d}/2S_i = -87.5$ cm^{-1}. In the crystal-field (CF) Hamiltonian in Eq. S4, $B^0_{2,i}$, $B^0_{4,i}$, and $|B^3_{4,i}|$ are the CF parameters appropriate for C_{3v} symmetry, while $\hat{O}^0_{2,i}$, $\hat{O}^0_{4,i}$, and $\hat{O}^3_{4,i}$ are the operator equivalents. The resulting best-fit CF parameters for the terminal C_{3v} chromophore are: $B^0_{2,i}$ = 212.3(12) cm^{-1}, $B^0_{4,i}$ = 55.32(10) cm^{-1} and $|B^3_{4,i}|$ = 577(4) cm^{-1}. The presence of other minima was excluded prior to the fit, performing an explorative survey over values of $B^0_{2,i}$, $B^0_{4,i}$, and $|B^3_{4,i}|$ between ±1000 cm^{-1}.

Table S6. Energy levels (cm^{-1}) obtained by AOM calculations on the idealized terminal chromophore with C_{3v} symmetry in **1Br**, with and without SO coupling.[a]

ζ_{3d} = 0 cm^{-1}		ζ_{3d} = 350 cm^{-1}			
^{5}E	0.000	1	0.000	14	6266.736
^{5}E	6277.700	2	0.042	15	6404.264
^{5}A$_1$	6526.556	3	56.274	16	6404.264
		4	56.274	17	6547.284
		5	118.480	18	6547.284
		6	118.480	19	6699.387
		7	171.469	20	6699.387
		8	205.604	21	6703.197
		9	261.633	22	6703.197
		10	261.633	23	6703.325
		11	6094.128	24	6722.306
		12	6094.128	25	6723.303
		13	6238.276		

[a]Interelectronic repulsion and SO coupling parameters: B = 850 cm^{-1}, C = 3100 cm^{-1}, ζ_{3d} = 0 or 350 cm^{-1} (see column headers), k = 1.0. LF parameters for C_{3v} chromophore: e_σ(py) = 6078 cm^{-1}, $e_{\pi\perp}$(py) = 150 cm^{-1}, e_σ(Br) = 3430 cm^{-1}, e_π(Br) = 1029 cm^{-1}.

In AOM calculations on the inner Fe centers (Fe2 and Fe3), all N-donor atoms were treated as pyridine-type donors, with e_σ(N) values estimated from Fe−N distances using Eq. S2 and setting

$e_\pi(N)/e_\sigma(N) = 0$.[2] As found in **1Cl**, both Fe2 and Fe3 have a well-isolated $S_i = 2$ orbital singlet, the first-order orbital momentum being quenched by the highly-distorted pentacoordinate environment.[2] Excited states lie at >1800 and >2300 cm^{-1}, respectively, and the $S_i = 2$ manifolds span an energy range of 35−46 cm^{-1} (Table S7). The pattern of energy levels indicates an easy-axis anisotropy, with a small or moderate rhombic distortion. Using PHI v3.0.6 code,[11] the five low-lying levels of Fe2 and Fe3 ($i = 2, 3$) were mapped on a giant-spin Hamiltonian:

$$\hat{H}_i = \hat{S}_i \cdot \bar{\bar{D}}_i \cdot \hat{S}_i + \mu_B B \cdot \bar{\bar{g}}_i \cdot \hat{S}_i \qquad \text{(S5)}$$

where $\bar{\bar{D}}_i$ and $\bar{\bar{g}}_i$ are the zero-field splitting (ZFS) and g tensors, respectively. The fit of the zero-field levels gave the axial (D_i) and rhombic (E_i) ZFS parameters. D_i is negative and large ($|D_i| = 8.8-11.3$ cm^{-1}), while rhombic distortion is moderate in Fe2 ($|E_2/D_2| = 0.11$) and small in Fe3 ($|E_3/D_3| = 0.02$). The values of D_i and E_i along with the principal directions of $\bar{\bar{D}}_i$ for each Fe center are listed in Table S8. The angle between the easy axis of Fe2 (Fe3) and the Fe2−Fe1 (Fe3−Fe4) direction is 82.4° (104.5°) and indicates that the easy direction of Fe2 (Fe3) is approximately perpendicular to the metal chain. In the same table we also list the g-values along the principal directions of the $\bar{\bar{D}}_i$ tensor, which were obtained from the field-dependence of the five low-lying levels. For simplicity, in all subsequent calculations the $\bar{\bar{D}}_i$ and $\bar{\bar{g}}_i$ tensors of Fe2 and Fe3 were assumed to be axial, with identical D_i parameters and principal g-factors, obtained as average values over the data in Table S8. Furthermore, the easy axes of Fe2 and Fe3 were taken as perpendicular to the threefold-symmetry axes of Fe1 and Fe4, respectively.

Table S7. Energy (cm^{-1}) of the low-lying levels obtained by AOM calculations on Fe2 and Fe3 in **1Br**.[a] Separations to the nearest excited levels are listed at the bottom of each column.

Fe2[b]		Fe3[c]	
1	0.000	1	0.000
2	0.465	2	0.104
3	30.518	3	25.956
4	38.043	4	27.101
5	46.158	5	35.443
	(>1800)		(>2300)

[a]Interelectronic repulsion and SO coupling parameters: $B = 850$ cm^{-1}, $C = 3100$ cm^{-1}, $\zeta_{3d} = 350$ cm^{-1}, $k = 1.0$. [b]LF parameters for Fe2: $e_\sigma(N4) = 5661$ cm^{-1}, $e_\sigma(N5) = 7926$ cm^{-1}, $e_\sigma(N6) = 7510$ cm^{-1}, $e_\sigma(N7) = 4692$ cm^{-1}, $e_\sigma(N8) = 2074$ cm^{-1}, $e_\pi/e_\sigma = 0$. [c]LF parameters for Fe3: $e_\sigma(N8) = 2035$ cm^{-1}, $e_\sigma(N9) = 3996$ cm^{-1}, $e_\sigma(N10) = 6851$ cm^{-1}, $e_\sigma(N11) = 6974$ cm^{-1}, $e_\sigma(N12) = 6012$ cm^{-1}, $e_\pi/e_\sigma = 0$.

Table S8. Magnetic parameters of Fe2 and Fe3 in **1Br** derived from AOM calculations and Eq. S5.

	Easy axis (z)[a]	Hard axis (x)[a]	Intermed. axis (y)[a]	D_i, E_i (cm^{-1})	$g_{x,i}$, $g_{y,i}$, $g_{z,i}$[b]
Fe2	82.41, 34.80	73.40, −57.48	161.66, −31.51	−11.31, 1.26	1.99, 2.06, 2.24
Fe3	104.52, 1.35	34.07, 68.83	59.94, −80.03	−8.85, 0.19	2.04, 2.03, 2.18

[a]Polar angles θ and ϕ (°) of the principal directions of the $\bar{\bar{D}}_i$ tensor (x,y,z) in a local reference frame (X,Y,Z) defined as follows: for Fe2, the Z axis is taken along Fe2–Fe1, with X along the projection of Fe2–N4 on the plane normal to Z; for Fe3, the Z axis is taken along Fe3–Fe4 direction, with X along the projection of Fe3–N12 on the plane normal to Z; in both cases Y is chosen so as to give a right-handed orthogonal coordinate system. [b]Values of the g-factor along the principal directions of the $\bar{\bar{D}}_i$ tensor.

Based on these single-ion properties, the magnetic behaviour of complex **1Br** was analyzed with the same procedure used for the chloro analogue **1Cl**.[2] The molecule was modelled in PHI v3.0.6[11] as two identical ferromagnetic Fe_2 pairs (Fe1,Fe2 and Fe3,Fe4) weakly antiferromagnetically coupled with each other. The Hamiltonians for the two pairs:

$$\hat{H}_{Fe1,Fe2} = J\hat{S}_1 \cdot \hat{S}_2 + \hat{H}_1 + \hat{H}_2 \quad \text{(S6)}$$

$$\hat{H}_{Fe3,Fe4} = J\hat{S}_3 \cdot \hat{S}_4 + \hat{H}_3 + \hat{H}_4 \quad \text{(S7)}$$

contain the intradimer ferromagnetic interaction (J < 0), which was treated following Lines' approach,[11,12] and the single-ion Hamiltonians $\hat{H}_i$ defined in Eqs. S3-S5. The single-ion parameters used in Eqs. S6 and S7 were as follows: for Fe1 and Fe4, $S_i = 2$, $L_i = 2$, $B^0_{2,i} = 212.3$ cm^{-1}, $B^0_{4,i} = 55.32$ cm^{-1}, $B^3_{4,i} = 577$ cm^{-1}, $\lambda_i = -87.5$ cm^{-1}; for Fe2 and Fe3: $S_i = 2$, $L_i = 0$, $B^0_{2,i} = D_i/3 = -3.359$ cm^{-1}, $B^2_{2,i} = E_i = 0$, $g_{x,i} = g_{y,i} = 2.03$, $g_{z,i} = 2.21$. The antiferromagnetic interdimer interaction ($J_{\text{eff}} > 0$) was treated in the mean-field approximation,[13] which is valid for $J_{\text{eff}} << |J|$. Thanks to this simplification, the size of Hilbert space collapses from 15625 × 15625 to 125 × 125, allowing for diagonalization of the Hamiltonian matrix and calculation of accurate powder averages with our computational resources. However, only susceptibility vs temperature data could be fitted, based on mean-field correction given by Eq. S8:

$$\chi = \frac{\chi_0}{1 + \frac{zJ_{eff}}{N_A \mu_B^2 g_{av}^2}\chi_0} \quad \text{(S8)}$$

where χ and χ_0 are the corrected and uncorrected susceptibility, respectively, $z = 1$ is the number of interacting nearest neighbours, and g_{av} is the temperature independent average g-factor of the Fe_2 unit. Notice that Eq. S8 differs slightly from that used in PHI v3.0.6[11] and that the best-fit zJ parameter appearing in PHI corresponds to $-zJ_{\text{eff}}/g_{\text{av}}^2$ in our treatment. Temperature-independent paramagnetism (TIP) was also included to accurately reproduce high-temperature data.

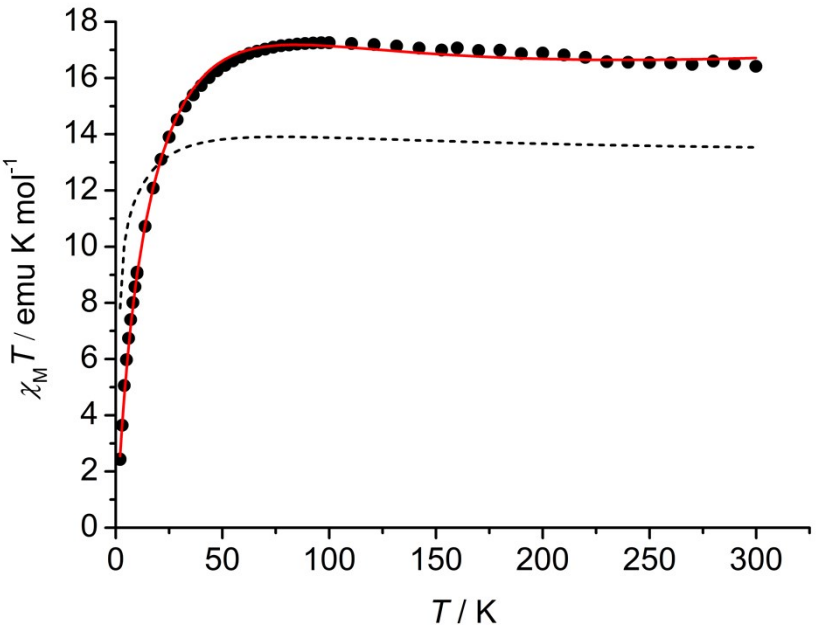

Figure S12. Experimental susceptibility data at H = 10 kOe (black dots) and best-fit curve (from AOM calculations, red line) for **1Br**·2.3CH_2Cl_2·Et_2O. The dashed line represents the simulated magnetic response of four uncoupled HS iron(II) ions, where LF parameters and g-values are fixed at the values obtained from AOM calculations.

9) Ab-initio Calculations

Table S9. Lowest-lying states for the four iron(II) ions in **1Cl** as determined by CASSCF-NEVPT2-SO calculations.

Fe1

Eigenvalues:	cm^{-1}	eV	Boltzmann population at T = 300.000 K
0:	0.00	0.0000	1.90e-01
1:	0.75	0.0001	1.90e-01
2:	27.33	0.0034	1.67e-01
3:	39.31	0.0049	1.58e-01
4:	48.48	0.0060	1.51e-01
5:	350.24	0.0434	3.55e-02
6:	360.14	0.0447	3.38e-02
7:	395.35	0.0490	2.86e-02
8:	437.06	0.0542	2.34e-02
9:	439.83	0.0545	2.31e-02

Fe2

Eigenvalues:	cm^{-1}	eV	Boltzmann population at T = 300.000 K
0:	0.00	0.0000	2.20e-01
1:	4.88	0.0006	2.15e-01
2:	16.55	0.0021	2.03e-01
3:	39.57	0.0049	1.82e-01
4:	40.74	0.0051	1.81e-01

Fe3

Eigenvalues:	cm^{-1}	eV	Boltzmann population at T = 300.000 K
0:	0.00	0.0000	2.15e-01
1:	6.42	0.0008	2.09e-01
2:	9.39	0.0012	2.06e-01
3:	31.35	0.0039	1.85e-01
4:	31.44	0.0039	1.85e-01

Fe4

Eigenvalues:	cm^{-1}	eV	Boltzmann population at T = 300.000 K
0:	0.00	0.0000	1.85e-01
1:	0.30	0.0000	1.84e-01
2:	49.00	0.0061	1.46e-01
3:	55.55	0.0069	1.41e-01
4:	81.05	0.0100	1.25e-01
5:	239.82	0.0297	5.84e-02
6:	260.42	0.0323	5.29e-02
7:	303.87	0.0377	4.30e-02
8:	362.40	0.0449	3.24e-02
9:	364.00	0.0451	3.22e-02

Table S10. Lowest-lying states for the four iron(II) ions in **1Br** as determined by CASSCF-NEVPT2-SO calculations.

Fe1

Eigenvalues:	cm^{-1}	eV	Boltzmann population at T = 300.000 K
0:	0.00	0.0000	1.93e-01
1:	0.98	0.0001	1.92e-01
2:	28.63	0.0036	1.68e-01
3:	42.18	0.0052	1.58e-01
4:	51.85	0.0064	1.51e-01
5:	359.79	0.0446	3.44e-02
6:	371.09	0.0460	3.26e-02
7:	408.02	0.0506	2.73e-02
8:	454.42	0.0563	2.19e-02
9:	457.17	0.0567	2.16e-02

Fe2

Eigenvalues:	cm^{-1}	eV	Boltzmann population at T = 300.000 K
0:	0.00	0.0000	2.20e-01
1:	4.70	0.0006	2.15e-01
2:	17.00	0.0021	2.03e-01
3:	39.72	0.0049	1.82e-01
4:	41.02	0.0051	1.81e-01

Fe3

Eigenvalues:	cm^{-1}	eV	Boltzmann population at T = 300.000 K
0:	0.00	0.0000	2.15e-01
1:	6.26	0.0008	2.09e-01
2:	9.30	0.0012	2.06e-01
3:	30.84	0.0038	1.85e-01
4:	30.93	0.0038	1.85e-01

Fe4

Eigenvalues:	cm^{-1}	eV	Boltzmann population at T = 300.000 K
0:	0.00	0.0000	1.93e-01
1:	0.45	0.0001	1.92e-01
2:	44.44	0.0055	1.56e-01
3:	54.25	0.0067	1.49e-01
4:	73.75	0.0091	1.35e-01
5:	298.72	0.0370	4.60e-02
6:	316.67	0.0393	4.22e-02
7:	357.13	0.0443	3.48e-02
8:	416.22	0.0516	2.62e-02
9:	418.09	0.0518	2.60e-02

Table S11. Angles (°) between the easy (e), intermediate (i) and hard (h) principal directions of the $\bar{\bar{D}}_i$ and $\bar{\bar{g}}_i$ tensors for each iron(II) ion in **1Cl** and **1Br**. Values for the main anisotropy axes are marked in bold.

	$[Fe_4(tpda)_3Cl_2]$ (**1Cl**)			$[Fe_4(tpda)_3Br_2]$ (**1Br**)		
	$i_{D,i}$, $i_{g,i}$	$h_{D,i}$, $h_{g,i}$	$e_{D,i}$, $e_{g,i}$	$i_{D,i}$, $i_{g,i}$	$h_{D,i}$, $h_{g,i}$	$e_{D,i}$, $e_{g,i}$
Fe1	6.07	4.05	**7.29**	5.70	3.61	**6.45**
Fe2	1.01	**1.16**	0.58	1.21	**1.22**	0.38
Fe3	43.20	**1.18**	43.19	44.14	**1.18**	44.13
Fe4	20.45	20.84	**4.07**	10.79	11.43	**3.79**

Supplementary Note 5: fitting of DC magnetic data. Several models differing in the constraints applied to J_{ij} values in Eq. 4 and in the refinement of a TIP correction were tested for their ability to simultaneously account for $\chi_M T$ vs T and M_M vs H data. The best-fit parameter sets so obtained are listed in Tables S12 and S13. We also carried out some fits on $\chi_M T$ vs T data only, as given in Table S14. Graphical material for selected models is available as Fig. S13-S17.

(a) In the simplest treatment, only nearest-neighbor super-exchange interactions were retained ($J' = 0$), and interactions within the Fe1,Fe2 and Fe3,Fe4 pairs were constrained to be equal ($J_{12} = J_{34}$). This model converges to ferromagnetic Fe1-Fe2 and Fe3-Fe4 couplings and to an antiferromagnetic Fe2-Fe3 interaction, and is thus qualitatively consistent with the results of DFT calculations.[2] However, even with the refinement of TIP correction, the magnetic response of both complexes on a high-energy scale ($\chi_M T$ vs T data) cannot be accurately reproduced (entries m**1X**A). As a cross check, this model remains unsatisfactory when M_M vs H data are excluded from the fit (entries m**1X**A').

(b) Allowing nonzero J' (while setting TIP = 0 to avoid overparameterization) gives two minima in the least-squares procedure, for either $J_{23} < 0$ and $J' > 0$, or vice versa. Both solutions have quite large $|J'|$ values (1.5-4.8 cm^{-1}) and are regarded as physically unlikely (entries m**1X**B, m**1X**C, m**1X**B' and m**1X**C').

(c) The condition $J_{12} = J_{34}$ was then relaxed. For **1Cl**, the improvement over m**1Cl**A is considerable with $J_{12} < J_{34} < 0$, $J_{23} > 0$ and a negligible TIP correction (entry m**1Cl**D). For **1Br**, both $J_{12} < J_{34} < 0$ and $J_{34} < J_{12} < 0$ (in either case with $J_{23} > 0$) give much improved fits as compared with m**1Br**A (entries m**1Br**D and m**1Br**E).

(d) Allowing J_{12} and J_{34} to be different while introducing next-nearest neighbor interactions (J') with TIP = 0 gives four distinct minima depending on the ordering of J_{12} and J_{34} and on the signs of J_{23} and J'. In **1Cl** (**1Br**) three (two) of these minima are regarded as physically unlikely ($|J'|$ = 1.8-3.9 cm^{-1}); the remaining ones (entries m**1Cl**G, m**1Br**G and m**1Br**I) have negligible $|J'|$ values and afford a comparable fit quality to the corresponding models with $J' = 0$ and TIP correction (entries m**1Cl**D, m**1Br**D and m**1Br**E, respectively).

It is important to note that the net coupling between the ferromagnetic Fe1,Fe2 and Fe3,Fe4 pairs, estimated as $J_{23}+2J'$, is invariably antiferromagnetic and remarkably constant across the explored models (3.7-5.1 cm^{-1} in **1Cl** and 2.9-4.6 cm^{-1} in **1Br**). The low temperature decrease of the $\chi_M T$ product is in fact primarily sensitive to this combined coupling term, and much less to the separate values of J_{23} and J'. Therefore, in what follows we disregard next-nearest neighbor interactions and further scrutinize models m**1Cl**D, m**1Br**D and m**1Br**E. Model m**1Cl**D unequivocally identifies the ordering of J_{12} and J_{34} in **1Cl**, namely $|J_{12}| > |J_{34}|$. Models m**1Br**D and m**1Br**E show that both

orderings yield a good reproduction of experimental data for **1Br**, the best mathematical solution being obtained with $|J_{34}| > |J_{12}|$ (m**1Br**E). On structural grounds, a reversed ordering of J_{12} and J_{34} in the two complexes is very unlikely. We thus contend that m**1Cl**D and m**1Br**D are the most plausible models for the two derivatives.

Table S12. Best-fit parameters from the simultaneous treatment of $\chi_M T$ vs T and M_M vs H data for **1Cl**·2.6CH_2Cl_2·0.84Et_2O.[a]

Model	J_{12}	J_{34}	J_{23}	$J' = J_{13} = J_{24}$	TIP	R
m**1Cl**A	−14.0(2)		4.404(17)	/	$8.0(2)\cdot10^{-3}$	322.4
m**1Cl**B	−23.74(14)		−3.31(3)	3.863(19)	/	44.6
m**1Cl**C	−26.11(15)		9.52(10)	−2.19(4)	/	102.5
m**1Cl**D	−51.4(10)	−9.43(5)	4.319(7)	/	$1.9(15)\cdot10^{-4}$	19.1
m**1Cl**E	−4.87(13)	−35.1(10)	4.48(3)	/	$5.7(2)\cdot10^{-3}$	325.8
m**1Cl**F	−51.6(4)	−10.53(10)	−3.29(4)	3.86(2)	/	6.5
m**1Cl**G	−52.0(3)	−9.76(10)	4.56(6)	−0.11(3)	/	18.6
m**1Cl**H	−7.32(15)	−55.7(6)	−2.44(4)	3.06(3)	/	22.0
m**1Cl**I	−13.87(15)	−46.4(4)	8.54(7)	−1.76(3)	/	45.3

[a] J values are in cm^{-1}, with $J > 0$ ($J < 0$) for antiferromagnetic (ferromagnetic) coupling; TIP is in emu mol^{-1}.

Table S13. Best-fit parameters from the simultaneous treatment of $\chi_M T$ vs T and M_M vs H data for **1Br**·2.3CH_2Cl_2·Et_2O.[a]

Model	J_{12}	J_{34}	J_{23}	$J' = J_{13} = J_{24}$	TIP	R
m**1Br**A	−9.31(16)		4.11(3)	/	$8.9(3)\cdot10^{-3}$	54.2
m**1Br**B	−18.7(4)		−4.48(15)	4.47(8)	/	151.7
m**1Br**C	−18.7(5)		7.5(2)	−1.47(10)	/	84.0
m**1Br**D	−26.8(14)	−4.61(15)	4.19(3)	/	$4.7(4)\cdot10^{-3}$	25.4
m**1Br**E	−3.61(3)	−38.6(11)	4.292(13)	/	$2.5(2)\cdot10^{-3}$	4.9
m**1Br**F	−54.6(10)	−2.2(3)	−1.7(2)	2.66(12)	/	122.3
m**1Br**G	−47.2(16)	−5.2(3)	4.59(16)	−0.14(7)	/	33.0
m**1Br**H	0.81(17)	−63.1(17)	−1.43(7)	2.17(4)	/	28.1
m**1Br**I	−4.25(14)	−52.4(6)	4.76(10)	−0.18(4)	/	6.8

[a] J values are in cm^{-1}, with $J > 0$ ($J < 0$) for antiferromagnetic (ferromagnetic) coupling; TIP is in emu mol^{-1}.

Table S14. Best-fit parameters from the treatment of $\chi_M T$ vs T data for **1Cl**·2.6CH_2Cl_2·0.84Et_2O and **1Br**·2.3CH_2Cl_2·Et_2O.[a]

Model	$J_{12} = J_{34}$	J_{23}	$J' = J_{13} = J_{24}$	TIP	R
m**1Cl**A'	−16.6(3)	4.33(3)	/	$5.7(2)\cdot10^{-3}$	31.4
m**1Cl**B'	−24.91(19)	−4.93(17)	4.79(9)	/	26.4
m**1Cl**C'	−26.16(15)	10.20(12)	−2.56(5)	/	12.2
m**1Br**A'	−9.4(2)	3.70(5)	/	$8.3(4)\cdot10^{-3}$	8.3
m**1Br**B'	−18.8(8)	−5.2(5)	4.8(3)	/	21.9
m**1Br**C'	−21.2(7)	10.9(6)	−2.8(2)	/	11.6

[a] J values are in cm^{-1}, with $J > 0$ ($J < 0$) for antiferromagnetic (ferromagnetic) coupling; TIP is in emu mol^{-1}.

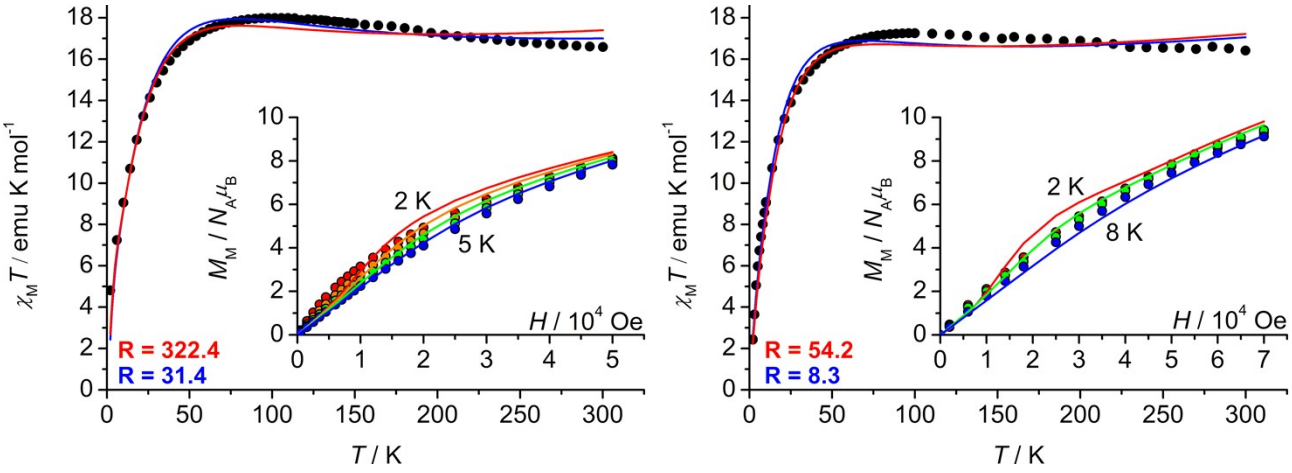

Figure S13. Best-fit curves (red lines) to the experimental data in Figure 8 based on model m**1Cl**A (left) and model m**1Br**A (right) (see Tables S12 and S13). The blue lines in the main panels are the best-fit curves from the treatment of $\chi_M T$ vs T data only, based on model m**1Cl**A' (left) and model m**1Br**A' (right) (see Table S14).

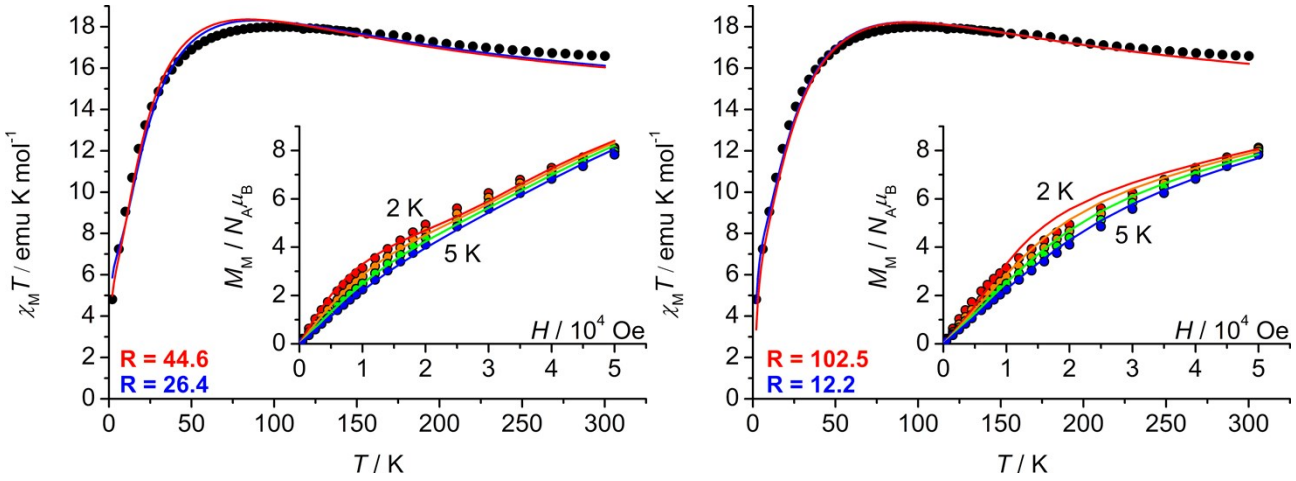

Figure S14. Best-fit curves to the experimental data in Figure 8(b) based on model m**1ClB** (left) and model m**1ClC** (right) (see Table S12). The blue lines in the main panels are the best-fit curves from the treatment of $\chi_M T$ vs T data only, based on model m**1ClB**' (left) and model m**1ClC**' (right) (see Table S14).

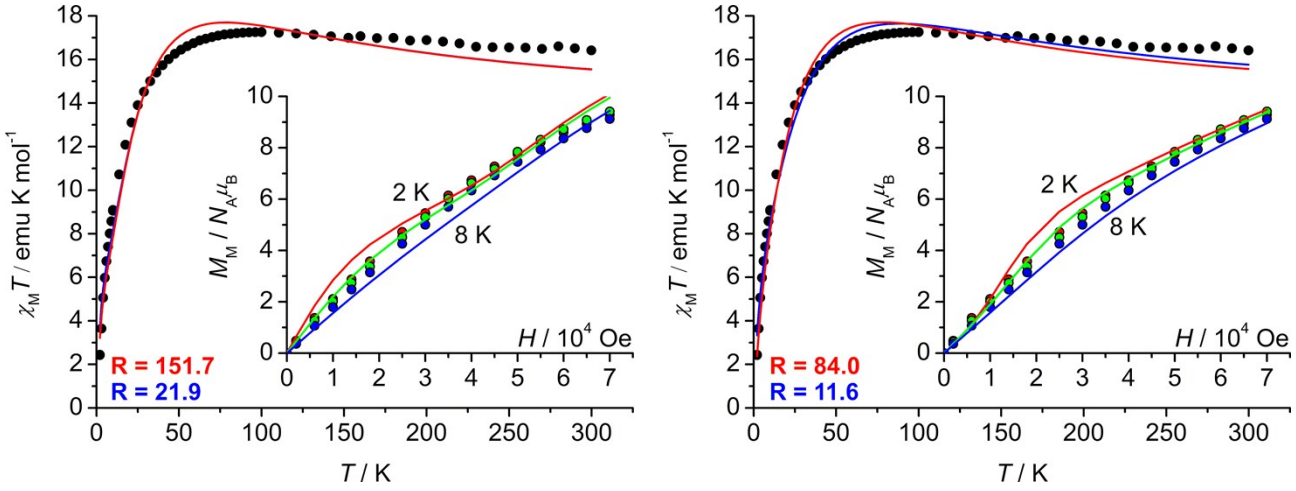

Figure S15. Best-fit curves to the experimental data in Figure 8(a) based on model m**1Br**B (left) and model m**1Br**C (right) (see Table S13). The blue lines in the main panels are the best-fit curves from the treatment of $\chi_M T$ vs T data only, based on model m**1Br**B' (left) and model m**1Br**C' (right) (see Table S14).

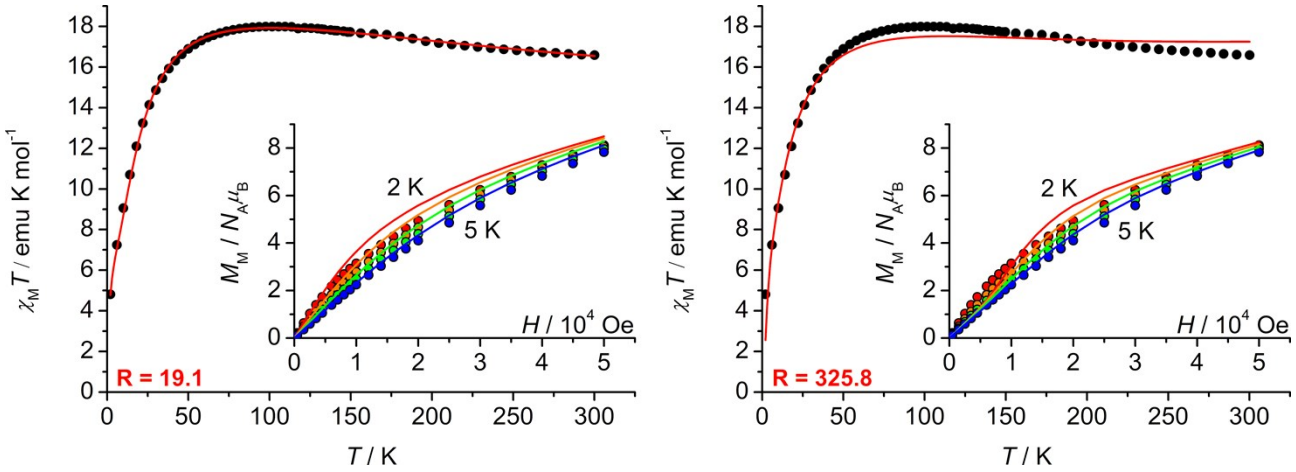

Figure S16. Best-fit curves to the experimental data in Figure 8(b) based on models m**1Cl**D (left) and m**1Cl**E (right) (see Table S12).

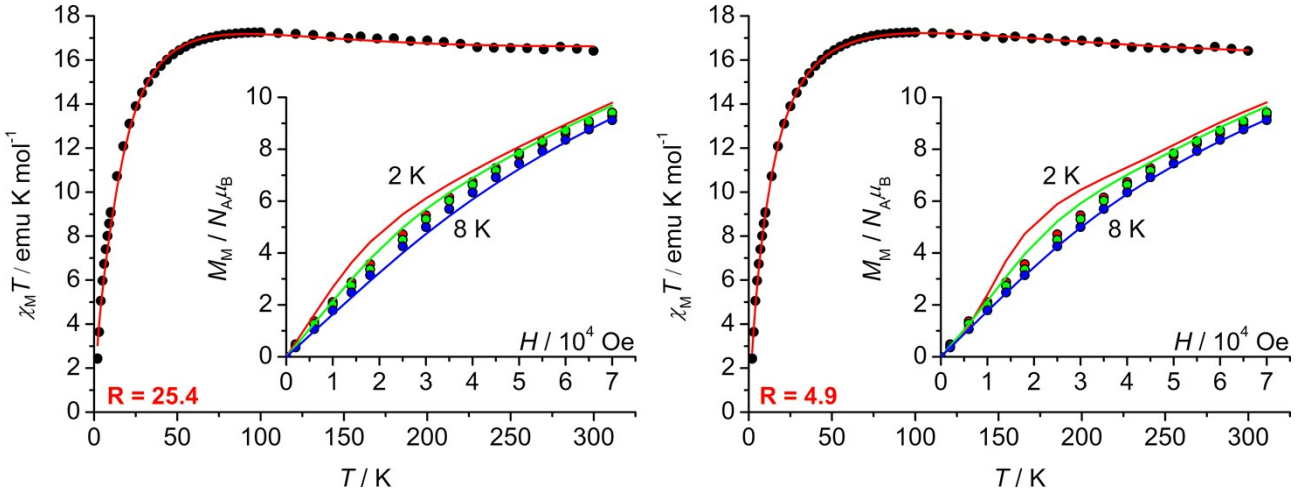

Figure S17. Best-fit curves to the experimental data in Figure 8(a) based on models m**1Br**D (left) and m**1Br**E (right) (see Table S13).

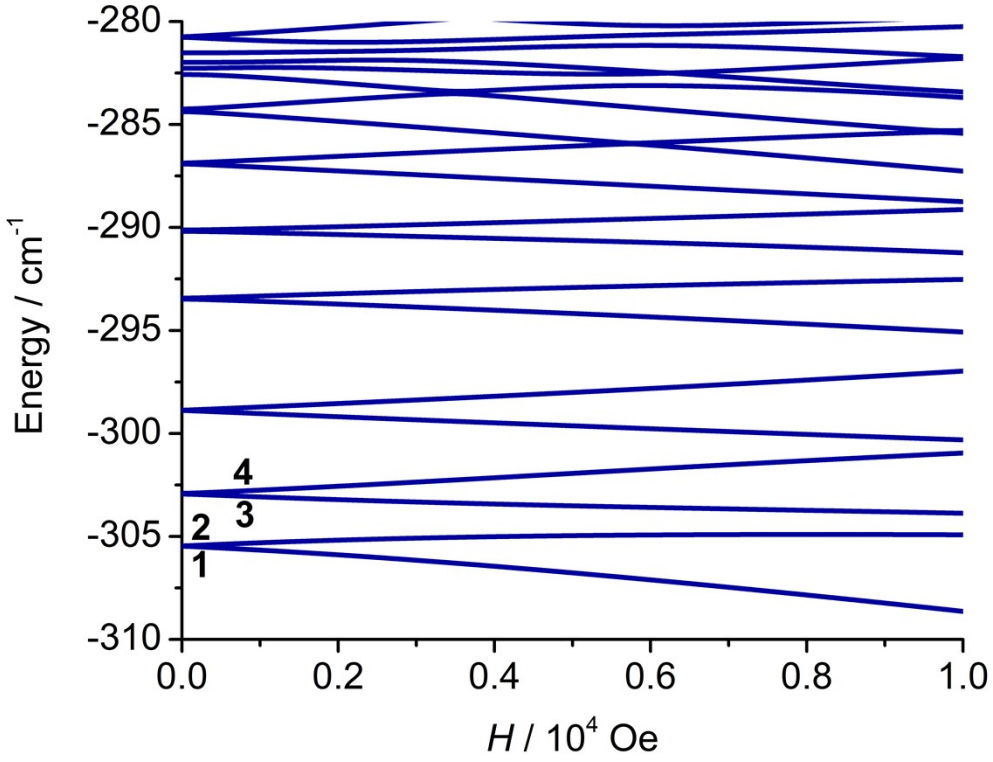

Figure S18. Zeeman diagram for **1Cl** when the magnetic field is applied along the direction of maximum splitting for the ground doublet (z_3).

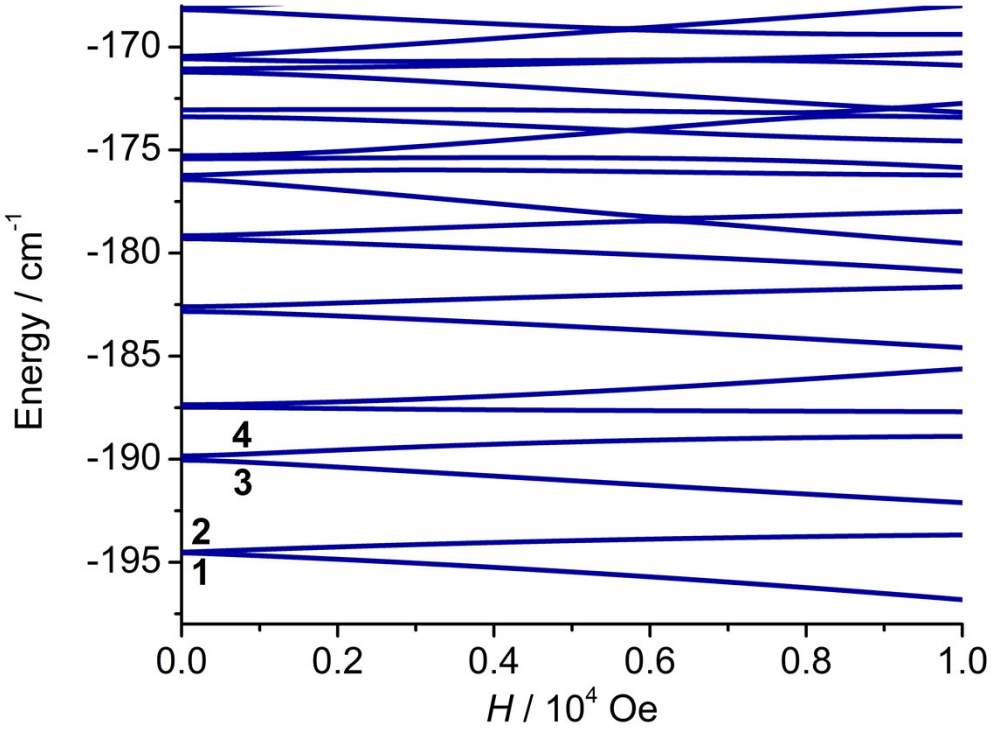

Figure S19. Zeeman diagram for **1Br** when the magnetic field is applied along the direction of maximum splitting for the ground doublet (z_3).

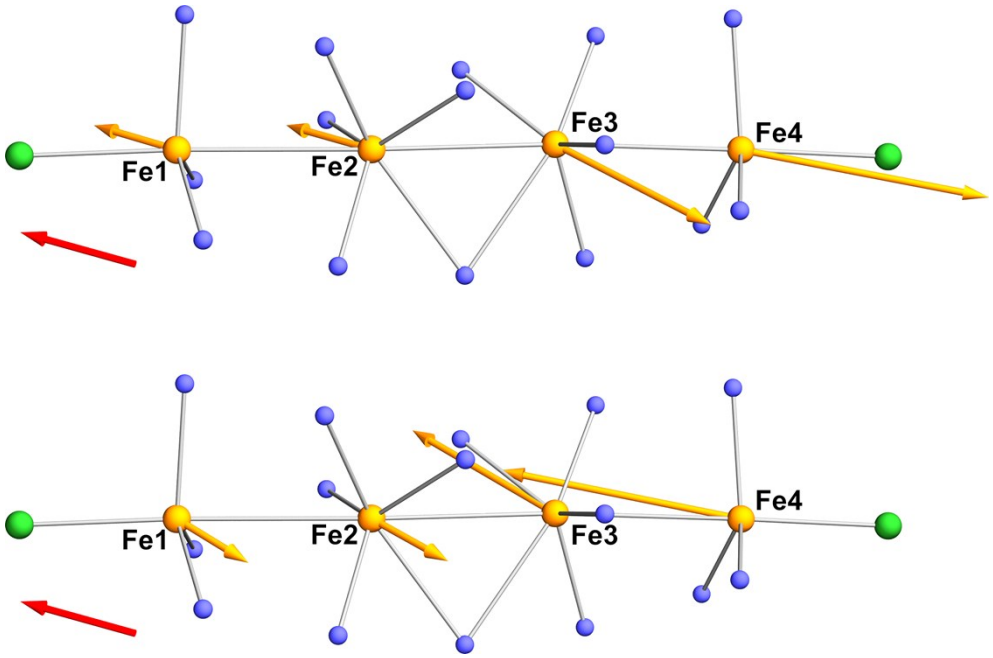

Figure S20. Local spin components (orange arrows, drawn on an arbitrary scale) in the first-excited doublet of **1Cl** when a 1-kOe magnetic field (red arrow) is applied along the direction of maximum Zeeman splitting (z_3'). The upper and lower panels picture states 3 and 4, respectively. Notice that in state 3 the spins on Fe1 and Fe2 are approximately parallel with each other, and antiparallel to the spin on Fe3; as compared with state 1, however, state 3 entails a much reduced spin on Fe1 and Fe2, in such a way that Fe1, Fe2, and Fe3 roughly cancel each other and the magnetic moment is primarily determined by Fe4. Same color code as in Figure 10.

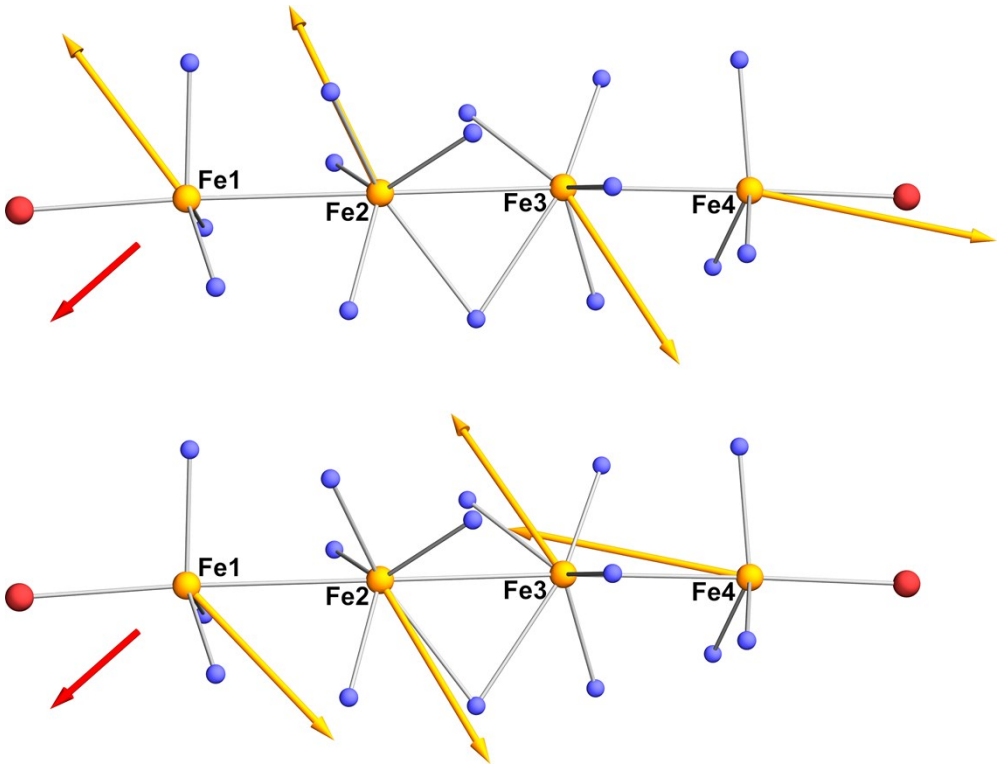

Figure S21. Local spin components (orange arrows, drawn on an arbitrary scale) in the ground doublet of **1Br** when a 1-kOe magnetic field (red arrow) is applied along the direction of maximum Zeeman splitting (z_3). The upper and lower panels picture states 1 and 2, respectively. Color code: orange, Fe; blue, N; red, Br.

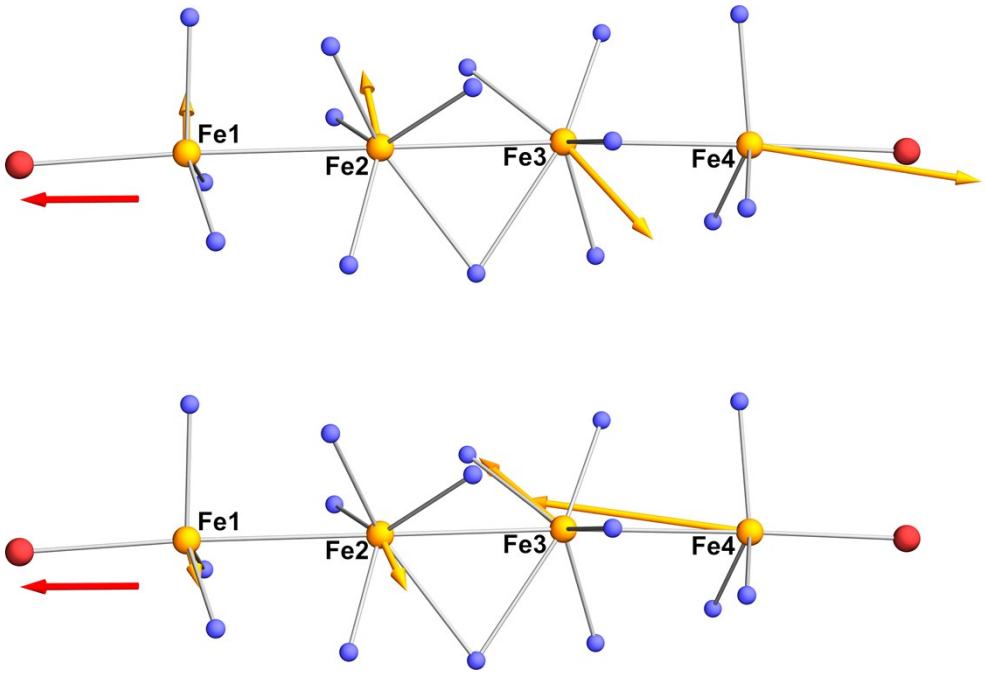

Figure S22. Local spin components (orange arrows, drawn on an arbitrary scale) in the first-excited doublet of **1Br** when a 1-kOe magnetic field (red arrow) is applied along the direction of maximum Zeeman splitting (z_3'). The upper and lower panels picture states 3 and 4, respectively. Same color code as in Figure S21.

Table S15. Spin moduli ($\hbar$), inter-spin angles (°) and angles between the spins and the chain axis Z (°) in state 1 of models m**1Cl**D and m**1Br**D.

Model	S_1	S_2	S_3	S_4	$S_1\hat{S}_2$	$S_2\hat{S}_3$	$S_3\hat{S}_4$	$S_1\hat{Z}$	$S_2\hat{Z}$	$S_3\hat{Z}$	$S_4\hat{Z}$
m**1Cl**D	1.53	1.61	1.82	1.99	6.1	162.8	34.9	66.7	71.0	121.7	155.9
m**1Br**D	1.63	1.74	1.77	1.97	14.5	171.1	47.2	56.3	69.7	113.5	159.1

10) AC Magnetic Measurements

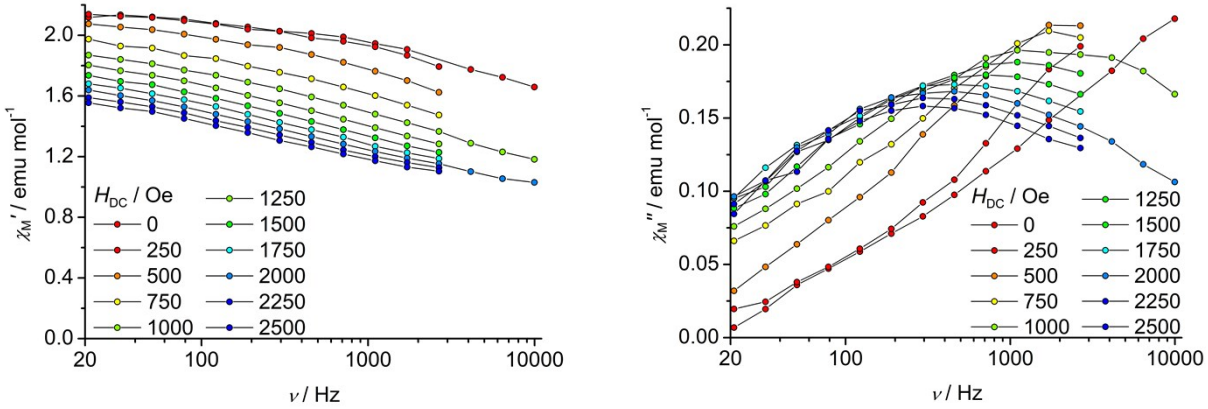

Figure S23. DC-field dependence of the in-phase (χ_M', left panel) and out-of-phase (χ_M'', right panel) components of molar magnetic susceptibility for **1Br**·2.3CH_2Cl_2·Et_2O at T = 2.0 K.

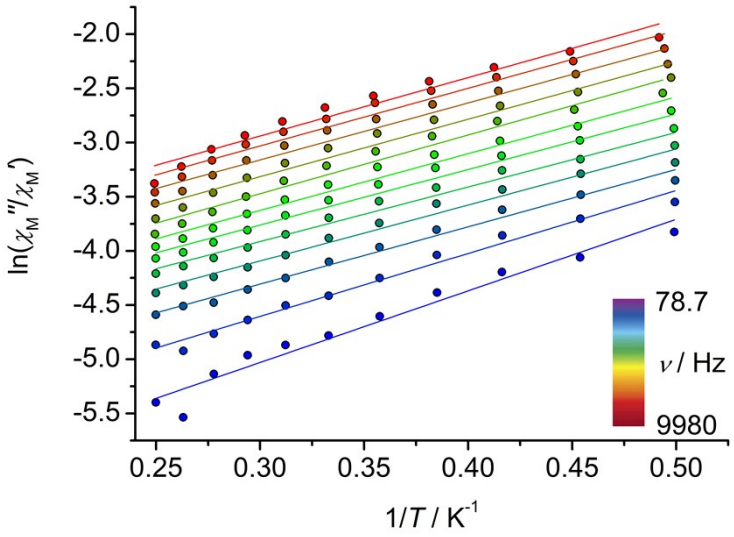

Figure S24. Frequency-dependent ln(χ_M''/χ_M') vs 1/T plots for **1Br**·2.3CH_2Cl_2·Et_2O (coloured dots) in zero DC field. The coloured lines represent the linear regression fits at each specific frequency (Eq. 5).

Table S16. Best-fit parameters obtained from the simultaneous treatment of χ_M'' and χ_M' vs ν data with the extended Debye model (Eqs. 7 and 8) for compound **1Br**·2.3CH_2Cl_2·Et_2O (H_{DC} = 1 kOe).

T / K	$\chi_{M,T}$ / emu mol^{-1}	$\chi_{M,S}$ / emu mol^{-1}	τ / μs	α
2.0	1.914(4)	0.904(11)	89(3)	0.514(7)
2.2	1.846(6)	0.89(2)	61(4)	0.526(11)
2.4	1.760(7)	0.88(3)	37(4)	0.530(15)
2.6	1.706(9)	0.83(5)	22(5)	0.56(2)
2.8	1.661(11)	0.77(9)	11(5)	0.61(3)
3.0	1.615(12)	0.75(13)	7(5)	0.63(3)

Table S17. Best-fit parameters obtained from the simultaneous treatment of χ_M'' and χ_M' vs ν data with the extended Debye model (Eqs. 7 and 8) for compound **1Br**·2.3CH_2Cl_2·Et_2O (H_{DC} = 2 kOe).

T / K	$\chi_{M,T}$ / emu mol^{-1}	$\chi_{M,S}$ / emu mol^{-1}	τ / μs	α
2.0	1.726(8)	0.886(10)	267(10)	0.513(10)
2.2	1.662(5)	0.902(7)	169(5)	0.474(8)
2.4	1.612(4)	0.903(9)	104(4)	0.465(9)
2.6	1.559(4)	0.906(13)	66(4)	0.450(12)
2.8	1.512(5)	0.90(2)	42(4)	0.443(18)
3.0	1.481(6)	0.86(4)	24(5)	0.48(3)

REFERENCES

1 Bruker, *TopSpin 4.0.6*, Bruker AXS Inc., Madison, Wisconsin, USA, 2018.

2 A. Nicolini, R. Galavotti, A.-L. Barra, M. Borsari, M. Caleffi, G. Luo, G. Novitchi, K. Park, A. Ranieri, L. Rigamonti, F. Roncaglia, C. Train and A. Cornia, *Inorg. Chem.*, 2018, **57**, 5438–5448.

3 J. Taylor, *Introduction to Error Analysis, the Study of Uncertainties in Physical Measurements*, University Science Books, New York, 2nd edn., 1997.

4 H. Adamsky (with contributions from P. E. Hoggard, M. Atanasov, K. Eifert), *AOMX*, http://www.aomx.de/docs/html/aomxeh.html (accessed May 2020).

5 A. Bencini, C. Benelli and D. Gatteschi, *Coord. Chem. Rev.*, 1984, **60**, 131–169.

6 B. F. Little and G. J. Long, *Inorg. Chem.*, 1978, **17**, 3401–3413.

7 R. Forgan, P. Tasker and F. White, *CCDC 1408270*, 2015, DOI:10.5517/cc1j8f29.

8 M. Gerloch, R. F. McMeeking and A. M. White, *J. Chem. Soc., Dalton Trans.*, 1975, 2452–2459.

9 G. J. Long and P. J. Clarke, *Inorg. Chem.*, 1978, **17**, 1394–1401.

10 A. B. P. Lever, *Inorganic Electronic Spectroscopy*, Elsevier, Amsterdam, 2nd edn., 1984.

11 N. F. Chilton, R. P. Anderson, L. D. Turner, A. Soncini and K. S. Murray, *J. Comput. Chem.*, 2013, **34**, 1164–1175.

12 M. E. Lines, *J. Chem. Phys.*, 1971, **55**, 2977–2984.

13 O. Kahn, *Molecular Magnetism*, VCH, New York, 1993.